Structure-property relationship of a soft colloidal glass in simple and mixed flows

Journal of Colloid and Interface Science 601 (2021) 454–466

Contents lists available at ScienceDirect

Journal of Colloid and Interface Science

journal homepage: www.elsevier.com/locate/jcis

Feature Article

Structure-property relationship of a soft colloidal glass in simple and mixed flows

Vincenzo Calabrese [a], Stylianos Varchanis [a,b], Simon J. Haward [a], John Tsamopoulos [b], Amy Q. Shen [a,*]

[a] Okinawa Institute of Science and Technology Graduate University, 1919-1 Tancha, Onna-son, Okinawa 904-0495, Japan
[b] Laboratory of Fluid Mechanics and Rheology, Department of Chemical Engineering, University of Patras, Patras 26500, Greece

GRAPHICAL ABSTRACT

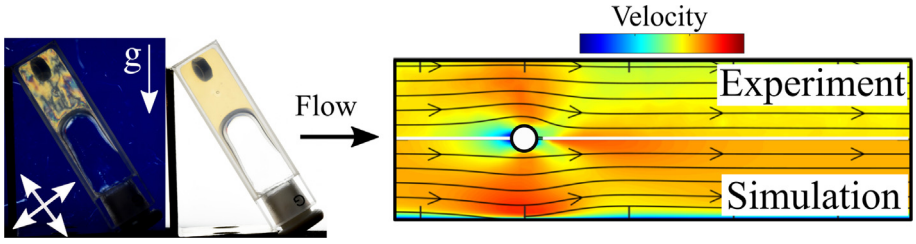

ARTICLE INFO

Article history:
Received 25 March 2021
Revised 17 May 2021
Accepted 18 May 2021
Available online 21 May 2021

Keywords:
Cellulose nanocrystals
Anisotropic soft materials
Microfluidics
Negative wake
Liquid crystal
Complex flows
Shear banding
Plasticity
Flow past a cylinder

ABSTRACT

Hypothesis: Under specific conditions, rod-like cellulose nanocrystals (CNC) can assemble into structurally ordered soft glasses (SGs) with anisotropy that can be controlled by applying shear. However, to achieve full structural control of SGs in real industrial processes, their response to mixed shear and extensional kinematics needs to be determined. We hypothesise that by knowing the shear rheology of the CNC-based soft glass and adopting a suitable constitutive model, it is possible to predict the structure-property relationship of the SG under mixed flows.

Experiments: We use an aqueous suspension with 2 wt% CNC at 25 mM NaCl to form a structurally ordered SG composed of a CNC network containing nematic domains. We combine rheometry and microfluidic experiments with numerical simulations to study the flow properties of the SG in shear, extension, and mixed flow conditions. Extensional flow is investigated in the Optimised Shape Cross-slot Extensional Rheometer (OSCER), where the SG is exposed to shear-free planar elongation. Mixed flow kinematics are investigated in a benchmark microfluidic cylinder device (MCD) where the SG flows past a confined cylinder in a microchannel.

Findings: The SG in the MCD displays a velocity overshoot (negative wake) and a pronounced CNC alignment downstream of the cylinder. Simulations using the thixotropic elasto-visco-plastic (TEVP) model yield near quantitative agreement of the velocity profiles in simple and mixed flows and capture the structural fingerprint of the material. Our results provide a comprehensive link between the structural behaviour of a CNC-based SG and its mechanistic properties, laying foundations for the development of functional, built-to-order soft materials.

* Corresponding author.
E-mail address: amy.shen@oist.jp (A.Q. Shen).

https://doi.org/10.1016/j.jcis.2021.05.103
0021-9797/

Contents

1. Introduction

The physical state of colloidal rods in suspension can be manipulated by modulating their concentration, particle aspect ratio, and the properties of the suspending fluid (i.e., the solvent), making colloidal rods versatile building blocks for soft materials [1–3]. In the limits of negligible inter-rod interactions, the particle aspect ratio l/d (where l and d are the length and diameter of the rod, respectively) is of primary importance to determine the phase behaviour of a colloidal rod suspension [1]. In the dilute regime, colloidal rods are uniformly distributed in the solvent and rarely interact, resulting in a rheological response dominated by the particle orientation [2]. Interparticle interactions are at play in the semidilute regime, as manifested by the onset of viscoelasticity and by a pronounced shear-thinning viscosity of the suspension [4,5]. At even greater concentrations, the motion of the particles becomes severely hindered, forming an isotropic glass phase or an ordered liquid crystal phase [1,6]. To further enrich the phase diagram of colloidal rods, particle surface charge and/or properties of the solvent fluid (e.g., pH, ionic strength) can be adjusted to modulate the balance between repulsive versus attractive interparticle forces. For instance, charged colloidal rods in the semidilute regime undergo an abrupt sol-to-gel transition above a critical ionic strength due to charge screening [7,8]. Colloidal gels and glasses display solid-like properties at rest and both consist of colloids in a dynamically arrested state with a pronounced elastic response [1,9,10]. However, the stress-bearing network in gels results from dominant attractive interparticle forces, forming fractal networks at relatively low concentrations [11]. Contrarily, the stress-bearing networks in glasses are usually identified by repulsive interparticle forces, at greater concentrations than those of gels [1,9,10]. Although microstructural fingerprints can be inferred for rod-like colloids in the suspension, the specific phase behaviour is accessible only when exact conditions of flexibility, surface chemistry, polydispersity, and aspect ratio of the particles are met.

Aqueous suspensions of rigid rod-like cellulose nanocrystals (CNC) have attracted much attention in the past decade because of their established industrial and academic significance [12–16]. Based on multiple experimental datasets reported in the literature, Xu et al. [17] recently presented a generalized phase diagram for CNC with different aspect ratios in an aqueous sodium chloride (NaCl) solution, by expressing the CNC concentration in a dimensionless form as $c = 0.25\pi l^2 dv$, referred to as Onsager's dimensionless concentration, where $v = N/V$ is the number of rods N per unit volume V.

In this work, we focus on a CNC-based structurally ordered soft glass (SG), recently referred to by Xu et al. [17–19] as "liquid crystal hydroglass", occurring at $0.1 < c < 0.8$ for NaCl concentrations in the range of 20–50 mM. These specific conditions of particle concentration and ionic strength sit in between the requisite for the formation of a gel and a glass. As such, the CNC assemble in a biphasic structure composed of ordered nematic CNC domains embedded within a weakly attractive CNC network. A similar structure as the liquid crystal hydroglass reported by Xu et al. [17–19] has been described by Bertsch et al. [16] using a 2 wt% CNC ($c \approx 0.3$) at a NaCl concentration of 20 mM, although they referred to it as "attractive glass containing nematic domains". Structurally ordered SG structures have been previously reported [15,20,21] in similar ranges of ionic strength and particle concentrations, although systematically investigated only recently [16,18]. It has been proposed that the coexisting structural ordering and stress-bearing network in an SG is the result of a balanced repulsive/attractive interparticle interplay, favouring the coexistence of nematic domains and particle caging [16,17]. Specifically, the presence of nematic domains within a glassy network occurs once the attractive and repulsive forces are balanced and the CNC display a ζ-potential of $\sim |30|$ mV [16]. Nematic order is lost at greater NaCl concentrations (> 50 mM) as excess charge screening leads to dominant associative forces, resulting in a stress-bearing network with an isotropic structure (ζ-potential $< |30|$ mV) [16]. At lower NaCl concentrations (< 20 mM), the

interparticle repulsive forces prevent the formation of stress-bearing networks and the suspension retains a liquid behaviour (ζ-potential $> |30|$ mV).

CNC-based structurally ordered SGs are yield stress materials which undergo a soft-solid to liquid-like transition beyond a critical imposed stress [15,16,19,21]. Upon shear, a fraction of the CNC composing the SG aligns, as generally observed for suspensions containing rod-like particles. However, once shear forces stop, the fast build-up of the attractive CNC network locks the shear-aligned CNC fraction in its orientation for a long time (e.g., days), hindering their relaxation towards isotropy [18,19]. This long-lasting, yet ultimately reversible, ordering of the CNC is a distinctive characteristic of SG and exploitable for the synthesis of soft materials with tunable anisotropy.

Even though pressure-driven flows and mixed shear and extensional kinematics are ubiquitously present in real industrial processes in which CNC-based SGs could be used for the synthesis of anisotropic soft solids (e.g. via 3D printing and fibre spinning), a comprehensive elucidation of the structure-property relationship of SG in flows relevant to industrial applications has not been achieved. In this work, we characterize the creeping flow behaviour of a CNC-based SG in shear, extension, and mixed flows using a combination of rheometric and microfluidic platforms. Specifically, we link flow visualization through micro-particle image velocimetry (μ-PIV) and flow-induced birefringence (FIB) experiments with constitutive modelling and numerical simulations to provide an extensive correlation between the microstructure of the SG and its rheological behaviour.

2. Experimental approach

2.1. Test fluid: SG

The test fluid, composed of a 2.0 wt% CNC at 25 mM NaCl, was prepared by diluting a stock aqueous CNC suspension (5.6 wt% CNC at pH 6.3, CelluForce, Montreal, Canada) with deionized water prior to the addition of the required NaCl solution (also prepared in deionized water) to reach a final NaCl concentration of 25 mM. After stirring, the suspension was equilibrated for at least 3 days before use. The CNC has an average length of $\langle l \rangle = 260 \pm 180$ nm and an average diameter of $\langle d \rangle = 4.8 \pm 1.8$ nm [22]. The 2.0 wt% CNC at 25 mM NaCl corresponds to the dimensionless Onsager concentration $c \approx 0.7$, when considering $\langle l \rangle$ and $\langle d \rangle$ as representative lengths of the CNC and a CNC density $\rho = 1560$ kg m^{-3} (where ρ is used to estimate the number density, ν) [23]. The value of $c \approx 0.7$ at 25 mM NaCl falls under the liquid crystal hydroglass phase in the phase diagram for CNC reported by Xu et al. [17], and in the glass phase according to the generalized phase diagram by Solomon and Spicer [1] (See ESI, Fig. S1). The CNC at 25 mM NaCl has a ζ-potential of $\simeq -30$ mV [16]. After *ca.* 2 h aging held upright, the test fluid displayed yield stress and birefringence (Fig. 1), features characteristic of the soft solid structure reported by Bertsch et al. for comparable CNC and NaCl concentrations [16]. Further references to "SG" imply the specific test fluid described above.

2.2. Rheological characterization

2.2.1. Shear rheometry

The shear rheology of the test fluid was measured using a strain-controlled ARES-G2 rotational shear rheometer (TA Instruments Inc.), equipped with a 50 mm stainless steel plate-plate geometry. The suspension was covered with a solvent trap and all the measurements were performed at 25 ± 0.1 °C (controlled via an advanced Peltier system). Following a 60 s pre-shear at 500 s^{-1}, oscillatory shear rheometry was conducted in the following order: (*i*) time sweep at constant angular frequency, $\omega = 1$ rad s^{-1}, and a constant strain amplitude $\gamma_0 = 0.1\%$; (*ii*) frequency sweep at $\gamma_0 = 0.1\%$; (*iii*) strain sweep at $\omega = 1$ rad s^{-1}. Flow curves were measured in steady-state upon a decreasing shear rate (500 to 10^{-3} s^{-1}) after a 60 s pre-shear at 500 s^{-1}.

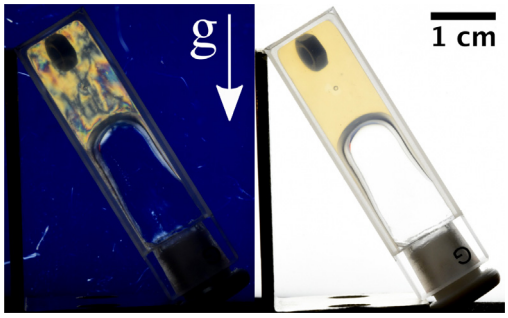

Fig. 1. Macroscopic appearance of the CNC-based SG (2.0 wt% CNC suspension at 25 mM NaCl) in a 1 cm wide quartz cuvette containing a metallic nut after *ca.* 2 h ageing upright. The picture on the left side is acquired placing the sample between two crossed polarizers.

2.2.2. Extensional rheometry

A capillary breakup extensional rheometer (CaBER 1, Thermo Scientific) was used to measure the filament thinning as a function of time (t). The test fluid was loaded between two plates (6 mm in diameter) located 1 mm apart. The plates were separated to a final gap of 6 mm with a constant velocity of 0.1 m s^{-1}. At 6 mm the two plates are sufficiently far apart for capillary forces to drive filament thinning and uniaxial extensional flow at the neck of the filament [24,25]. The time at which the plates reached their final gap was used as a reference ($t = 0$).

2.3. Microfluidic platforms

The optimized shape cross-slot extensional rheometer (OSCER) and a microfluidic cylinder device (MCD) were used to generate two-dimensional (2D) flows that provide pure extensional and mixed kinematics, respectively (Fig. 2). The OSCER (Fig. 2a,b) is a special cross-slot geometry developed by Haward et al. [26,27] that produces shear-free planar elongation in a large region around the stagnation point ($x = y = 0$ mm). The OSCER has characteristic dimensions of height $H = 2.1$ mm (z-axis) and width $W = 0.2$ mm at the inlets and outlets of the geometry (Fig. 2a). The fluid elements are compressed along the y-axis (compression axis) and extended along the x-axis (elongation axis). The MCD (Fig. 2c,d) consists of a straight channel with a rectangular cross-section of length $L = 25$ mm (x-axis), width $W = 0.4$ mm (y-axis) and height $H = 2$ mm (z-axis) containing, at a distance $L/2$ from the inlet, a rigid microcylinder of radius $R = 20$ μm and height H. The MCD was fabricated in fused silica glass by selective laser-induced etching (SLE) [28]. This technique enables the fabrication of optically transparent 3D structures with a high modulus (≈ 75 GPa) and a resolution of ≈ 1 μm [28,29]. The same MCD as the one reported herein has been employed in numerous experiments and described in detail therein [29–32]. Both geometries provide a relatively large aspect ratio $\alpha = H/W \geqslant 5$, generating a good approximation of 2D flow.

2.4. Flow control

The test fluid was driven inside the channels by Nemesys low-pressure syringe pumps (Cetoni GmbH) equipped with Hamilton

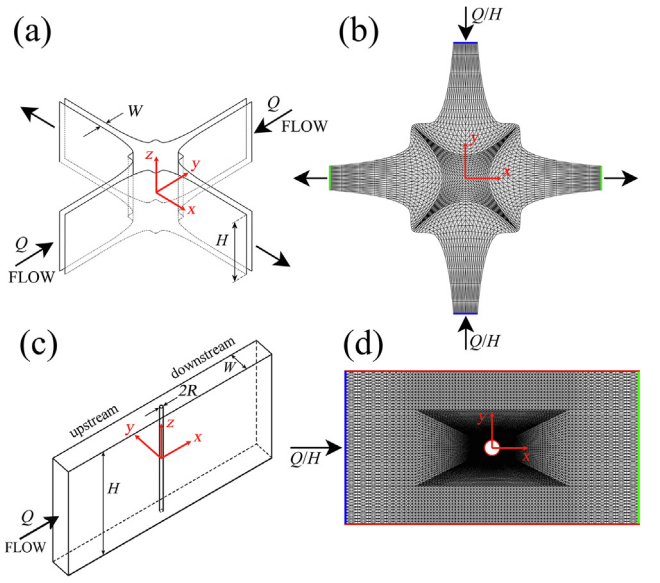

Fig. 2. (a) Schematic of the OSCER experimental setup and (b) its indicative discretization mesh used in the numerical simulation. (c) Schematic of the MCD experimental setup and (d) its indicative discretization mesh used in the numerical simulation.

Gastight syringes. The fluid was simultaneously infused at the inlet(s) and withdrawn from the outlet(s) with an equal volumetric flow rate ($Q = UWH$, where U is the average flow velocity). To ensure a consistent time history of the material, the test fluid was, (*i*) pre-flowed for 5 ± 1 s at a relatively high flow rate and (*ii*) equilibrated for 10 ± 1 s at the flow rate of interest prior to velocimetry and birefringence measurements (see Sections 2.5 and 2.6, respectively). The pre-flow protocol in (*i*) was conducted at a steady flow rate corresponding to $U = 0.03$ m s^{-1} and $U = 0.016$ m s^{-1} for the OSCER and MCD, respectively.

2.5. Micro-particle image velocimetry (μ-PIV)

The μ-PIV measurements were conducted using a volume illumination system (TSI Inc.) mounted on an inverted microscope (Nikon Eclipse Ti). The test fluid was seeded with 1.1 μm diameter fluorescent particles (Fluoro–MaxTM, Thermo Fisher) to a concentration of ≈ 0.02 wt%. The fluid was imaged using 4× and 10× objective lenses (Nikon PlanFluor), yielding measurement depths of 150 and 35 μm (equivalent to $\approx H/13$ and $\approx H/57$) for the OSCER and MCD, respectively [33]. Each geometry was imaged with the *z*-axis parallel to the light source and a sequence of at least 100 image pairs were acquired at the midplane of the geometry ($z = 0$ mm, see coordinate system defined in Fig. 2(a)(c)). For each imposed flow rate, the average displacement of the seeding particles between the two images in each pair was kept constant at ≈ 4 pixels. The cross-correlation between image pairs provided a square grid containing velocity vectors $\mathbf{u} = (u_x, u_y)$ with a spatial resolution of 32 and 12.8 μm/pixel for the OSCER and MCD, respectively.

2.6. Flow-induced birefringence (FIB)

FIB was measured using an Exicor MicroImager (Hinds Instruments Inc.) operating with a monochromatic light of wavelength $\lambda_w = 630$ nm. The geometries were imaged using 2× and 5× objective lenses and imaged in the same position as that described for the μ-PIV. The instrument performs Mueller matrix decomposition (4×4 Mueller matrices) to determine the retardance, δ, and the orientation of the slow optical axis, θ (extraordinary ray), from a total of 7 images acquired at 1 frame/s. The δ, describing the total phase shift between orthogonally polarized light beams, was accessible in the range between 0 and π. It is noted that δ is directly proportional to the birefringence intensity as $\Delta n \approx \delta\lambda_w/(2\pi H)$. As the SG displayed inhomogeneous retardance at rest (due to the presence of the nematic domains), the background value of δ was determined for the geometries containing water and subtracted for all the analysis presented; this being a similar value to the instrument detection limit. The spatial resolution of the measurements were ≈ 5 μm/pixel and ≈ 2 μm/pixel for the 2× and 5× objective lenses, respectively.

3. Theoretical approach

3.1. Definition of the physical problem

In the numerical simulations, we consider the 2D creeping flow of the SG in the OSCER (see Fig. 2)) and in the MCD (see Fig. 2(c)-(d)). The material is incompressible with constant density ρ, plastic viscosity η_p, elastic modulus G, and yield stress τ_y. Regarding the OSCER (see Fig. 2(a)-(b)), the width of the inflow and outflow channels is denoted by W, the length of the channel is $L = 20W$. In all simulations, the flow domain spans $-20.5 \leqslant x/W \leqslant 20.5, -20.5 \leqslant y/W \leqslant 20.5$. As can be seen in Fig. 2(b), the origin of the axes is placed at the stagnation point that is formed at the center of the OSCER. As for the flow in the MCD (Fig. 2(c)-(d)), the width of the channel is denoted W and the radius of the cylinder R. The length of the channel is $L = 250R$, and in all simulations, the flow domain spans $-125 \leqslant x/R \leqslant 125, -10 \leqslant y/R \leqslant 10$. Fig. 2(d) shows the computational MCD flow geometry where the coordinates x and y correspond to the local streamwise velocity and its normal direction, respectively.

For both simulation and experiment, we scale all lengths with the characteristic length ℓ ($\ell = W$ for the OSCER and $\ell = R$ for the flow past a cylinder), velocities with the average flow velocity at the inflow U, and times with the characteristic inverse deformation rate ℓ/U. In addition, both the pressure and stress components are scaled with a viscous scale, $\eta_p U/\ell$. Thus, the dimensionless groups that arise are the Weissenberg number, $Wi = \eta_p U/(G\ell)$, and the yield strain, $\varepsilon_y = \tau_y/G$.

3.2. Governing equations

The non-Newtonian flow is described by the incompressible and isothermal Cauchy equations coupled with the constitutive equation, which accounts for the contribution of the non-Newtonian stresses. Neglecting inertia, the forms of the continuity, momentum, and constitutive equations are expressed in dimensional form, respectively, as

$$\nabla \cdot \mathbf{u} = 0, \tag{1}$$

$$\nabla \cdot (-P\mathbf{I} + \boldsymbol{\tau}) = \mathbf{0}, \tag{2}$$

$$\mathbf{f}(\boldsymbol{\tau}, \dot{\boldsymbol{\gamma}}) = \mathbf{0}, \tag{3}$$

where $\mathbf{u}$ is the velocity vector, P is the thermodynamic pressure, $\mathbf{I}$ is the identity tensor, and $\boldsymbol{\tau}$ is the non-Newtonian contribution to the total stress tensor. The deformation rate tensor $\dot{\boldsymbol{\gamma}}$, is defined as

$$\dot{\boldsymbol{\gamma}} = \nabla\mathbf{u} + (\nabla\mathbf{u})^T, \tag{4}$$

where the superscript "T" denotes the transpose operator. The usual no-slip and no-penetration boundary conditions (i.e., $\mathbf{u} = \mathbf{0}$) are

imposed on the cylinder surface and channel walls. Because the constitutive equation incorporates a stress diffusion term (see Eqs. 5, 6) we impose no-flux conditions (i.e., $\mathbf{n}\cdot\nabla\boldsymbol{\tau}=\mathbf{0}$) at all solid boundaries, with $\mathbf{n}$ denoting the normal, outward pointing vector on each solid boundary. At the inflow boundaries, we impose fully developed velocity and stress fields. In order to eliminate any additional numerical error that could arise due to the truncation of the domain, the open boundary condition (OBC) [34] has been applied along the outflow boundaries. According to the OBC, the fluid velocities and stresses are not imposed at the outflow boundary but are calculated from the weak form of the equations (extrapolated from the bulk). The form of the operator $\mathbf{f}$ is discussed in detail in the next section.

3.3. Rheological description of the test fluid (SG)

To describe the rheological behaviour of the test fluid we employ a simplified version of the nonlinear constitutive equation recently proposed by Varchanis et al. [35]. The aforementioned constitutive model, referred to as the TEVP model, is a very general phenomenological constitutive equation that can describe a wide class of thixotropic elasto-visco-plastic (TEVP) materials and is based on previous models by Saramito [36] and Dimitriou and McKinley [37]. The set of the simplified equations that relate the stress to the deformation rate tensor are given as:

$$\frac{1}{G_t}\left[\frac{D\boldsymbol{\tau}}{Dt}-(\nabla\mathbf{u})^T\cdot\boldsymbol{\tau}-\boldsymbol{\tau}\cdot\nabla\mathbf{u}\right]+ Y_{PTT}\max\left(0,\frac{\tau_D-\tau_y}{\eta_t\tau_D}\right)\boldsymbol{\tau}-\frac{D}{G_t}\nabla^2\boldsymbol{\tau}=\dot{\boldsymbol{\gamma}}, \tag{5}$$

$$\frac{D\lambda}{Dt}=k_1(1-\lambda)-k_2|\dot{\boldsymbol{\gamma}}_{\mathbf{vp}}|(\lambda-\lambda_\infty)+D\nabla^2\lambda. \tag{6}$$

Here λ is a non-dimensional structure parameter, which is introduced to indicate the instantaneous degree of "structure" in the material. It varies in a predetermined range with limits corresponding to the two extreme cases regarding the rheological response of the material. More specifically, when $\lambda=1$, the material is assumed to behave as an elastic solid; when $\lambda\to\lambda_\infty$, the material behaves like a weakly viscoelastic fluid. A detailed description of the role of the structure parameter and its application to structural kinetics models of thixotropy is given by Larson and Wei [40]. For the SG this corresponds to intact nematic domains within a fully structured CNC network at $\lambda=1$, and fluidized individual CNC for $\lambda\to\lambda_\infty$. The magnitude of the deviatoric stress tensor of $\boldsymbol{\tau}$ is denoted as $\tau_D=|\boldsymbol{\tau}-tr(\boldsymbol{\tau})\mathbf{I}/tr(\mathbf{I})|$, where $tr(\mathbf{A})$ denotes the trace of any tensor $\mathbf{A}$. The destruction rate of the nematic domains and the CNC network is proportional to the magnitude of the viscoplastic part of the deformation rate $|\dot{\boldsymbol{\gamma}}_{\mathbf{vp}}|=Y_{PTT}\max\left(0,\frac{\tau_D-\tau_y}{\eta_t\tau_D}\right)\boldsymbol{\tau}$. The Phan-Thien Tanner (PTT) function, which mainly governs the magnitude of the normal stresses, is defined as $Y_{PTT}=e^{\varepsilon tr(\boldsymbol{\tau})/G}$, with ε denoting the PTT parameter [41]. The material derivative is denoted as $D/Dt=\partial/\partial t+\mathbf{u}\cdot\nabla$. A stress diffusion term is added to the model to account for a continuous transition between the bands, when the flow is shear banded [42]. The additional material parameters of the model are: the thixotropic viscosity ($\eta_t=\eta_p\lambda^m$), which depends on the plastic viscosity η_p and the structure parameter λ, where m is a power exponent, the thixotropic elastic modulus (G_t), which depends on the elastic modulus and the structure parameter ($G_t=G(\lambda-\lambda_\infty)^n$, where n is another power exponent), the stress diffusivity (D), and the constants k_1 and k_2 which govern the magnitude of the structural build-up and breakage of the microstructure of the material (composed of nematic domains and CNC network), respectively. Thus, the TEVP model features 10 material parameters. The reason that we define the thixotropic viscosity (η_t) to depend on λ, while the thixotropic elastic modulus (G_t) to depend on $\lambda-\lambda_\infty$, is related to the structural rearrangements in the material at high deformation rates. As $\lambda\to\lambda_\infty$ the structure of the nematic domains and the CNC network is destroyed, leading to the flow of individualized rods, corresponding to a viscosity plateau (slightly higher than that of the solvent) and a vanishing elasticity. The latter argument can be supported by the fact that elasticity in elasto-visco-plastic (EVP) systems stems from the self-interacting building blocks of the microstructure resulting in a stress-bearing network [43]. When this network starts to collapse, the physical interactions within the microstructure weaken, and as a result, elasticity diminishes entirely. As we can observe in Eqs. 5 and 6, when the magnitude of the deviatoric stress tensor attains values lower than the yield stress, the von Mises criterion is not satisfied, and the material behaves as a purely hyperelastic material. When the yield stress is exceeded, the material starts to flow, behaving as a thixotropic viscoelastic fluid, whose plastic viscosity and elastic modulus depend on the deformation history, according to the isotropic hardeningmechanism. All material parameters of the model, except for the stress diffusivity, are estimated by performing simultaneous nonlinear regression [34,44] of the model to the oscillatory shear rheology (see Fig. 3)) the steady flow curve (Fig. 4(a)) of the material. The values yield the best fit with the experimental data of the SG are summarized in Table 1. In the absence of experimental measurements of the stress diffusivity, D, in the test fluid, we assign a particular value (see Table 1) so that

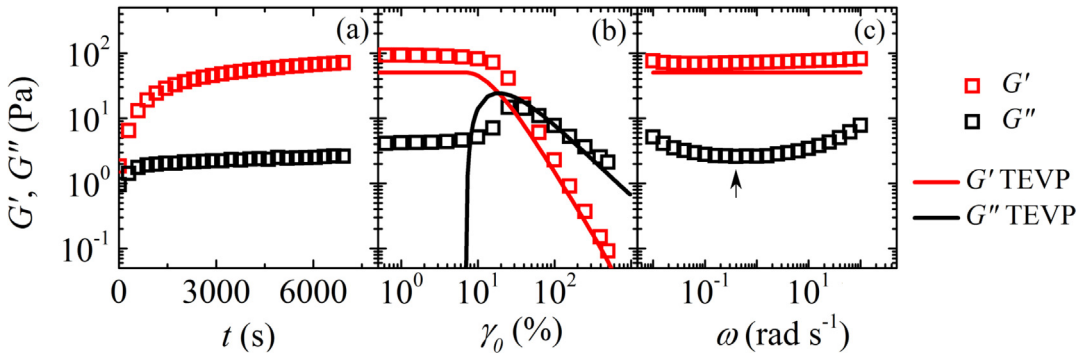

Fig. 3. (a) Time sweep at constant angular frequency, $\omega=1$ rad s^{-1}, and constant strain amplitude $\gamma_0=0.1\%$, (b) strain sweep at $\omega=1$ rad s^{-1} and (c) frequency sweep of the SG at $\gamma_0=0.1\%$. The arrow in (c) points to G'' at $\omega=0.4$ rad s^{-1}. The legend on the side applies to all three subfigures. Symbols and lines correspond to experimental data and predictions of the model, respectively. The predicted G' and G'' as a function of γ_0 in (b) are obtained by assuming homogeneous shear in the yx-direction and numerical time integration of Eqs. 5, 6.

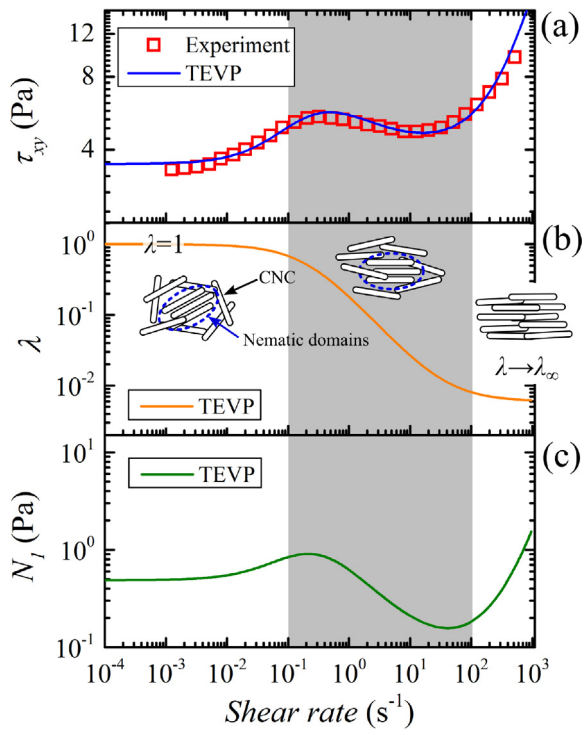

Fig. 4. Steady simple shear results for the SG. (a) Shear stress versus shear rate, (b) Structure parameter (λ) versus shear rate. (c) First normal stress difference (N_1) versus shear rate. The schematics in (b) display the structural organization of the SG under different shear rate regimes.

the dimensionless stress diffusivity ($D^* = D\eta_p/(GW^2)$) attains values $D^* \sim 0.001$ in both flow geometries that we examined [38]. Note that the value of D is also consistent with measurements of the stress diffusion coefficient in wormlike micellar solutions [39]. The governing equations (Eqs. 1,2,5,6) are discretized and solved with the Petrov-Galerkin stabilized finite element method for viscoelastic flows (PEGAFEM-V) [45,46]. The variational formulation along with details on the implementation and numerous benchmark tests are given by Varchanis et al. [45,46]. The mesh used in the OSCER simulations consisted of 144000 triangular elements while the size of the element at the stagnation point equals to $0.025H$. The characteristics of the mesh (M2) used in the MCD simulations are given by Varchanis et al. [32].

4. Results and discussion

In this section, we present and analyse the rheological response of the SG under different flow conditions. Initially, we examine homogeneous flows to understand the behaviour of the material under simple shear and extensional flow conditions, and relate the rheological properties to macroscopic variables of the constitutive model. Subsequently, we proceed to complex flows, in which the material is exposed to mixed and inhomogeneous flow fields characterized by shear and extensional kinematics, and evaluate the material response considering simultaneously the phenomena described in the simple shear and extensional flow.

4.1. Homogeneous flow

4.1.1. Oscillatory shear rheology

CNC glasses as well as CNC-based hydrogels have been recognized for their time-dependent rheological behaviour [16,18]. Therefore, we begin by probing the aging of the material (after 60 s pre-shear conducted at 500 s^{-1}) by following the storage and loss modulus, G' and G'', respectively, over time (Fig. 3(a)). A sharp elasticity build-up occurs at $0 < t < 10^3$s ($G' > G''$), followed by a slower and more gradual increase at longer times, as similarly reported by Bertsch et al. for CNC suspensions in the glass regime [16]. This time-dependent elasticity build-up has been ubiquitously observed in physically-crosslinked hydrogels [16,47]. For the specific case of the SG, the elasticity build-up is associated with the time scale required to develop its biphasic structure: a stress-bearing network containing nematic domains. The amplitude sweep (Fig. 3(b)) displays a linear viscoelastic region at small deformations ($\gamma_0 < 10\%$) where the moduli are independent of the magnitude of deformation. At larger deformations, the material enters a non-linear regime (γ_0-dependent moduli), where it yields and acquires a liquid-like behaviour ($G'' > G'$). At the crossover of G' and G'', a clear overshoot in G'' is evident. This type of moduli dependence on the deformation is referred to as a weak strain overshoot [48,47] and has been associated with the energy dissipation under plastic deformation [49]. It is clear from Fig. 3(b), that the TEVP model (solid lines) does not predict viscous dissipation in the linear regime. This is a well-known drawback of any elasto-visco-plastic model that adopts the max() formulation shown in Eq. 5 [36] for the transition from the solid state to the liquid state [35], and is related to the purely elastic modelling of the solid state. However, since the material does not flow when it is in the solid state, this discrepancy does not affect notably the rheological description of the material when flowing in a microfluidic device (discussed in Section 4.1.4 and 4.2) [43]. As the nonlinear regime is approached ($\gamma_0 \approx 10\%$), and the material yields (crossover of G' and G''), we observe a progressively improved match between the experimental data and the model. Within the nonlinear regime, $\gamma_0 \geqslant 30\%$, the experimental data are well described by the TEVP model.

Finally, a frequency sweep of the aged SG in the linear regime displays a constant G' versus angular frequency (Fig. 3(c)), as also predicted by the model. Notably G'' displays a minimum at $\omega \simeq 0.4$ rad s^{-1} (arrow shown in Fig. 3(c)), which has been associated with the characteristic thermal binding-unbinding rate of the physically cross-linked network junctions [50].

4.1.2. Steady shear rheology

Further insight regarding the SG's response upon non-linear deformations was captured by the flow curve in Fig. 4(a) where the shear stress, τ_{xy}, is plotted against the shear rate, $\dot{\gamma}$. The test fluid reached a fully destructured state by a pre-shear protocol before being measured in steady-state with a decreasing shear rate ramp. The decreasing shear rate ramp procedure removed "sample memory" effects (more details in Fig. S2, ESI), ensuring consistent measurements and consistency with the protocol adopted for the microfluidic experiments. In analogy to the shear-induced structural changes proposed by Xu et al. [19], we interpret the flow

Table 1
Set of parameters of the TEVP model for the description of the SG.

G (Pa)	η_p (Pa s)	τ_y (Pa)	ε	m	n	λ_∞	k_1 (s^{-1})	k_2	D (m^2/s)*
50	26	3.5	0.5	1.48	0.4	0.006	0.015	0.07	1.3×10^{-10}

* The value of D is assigned based on experimental and theoretical works of shear-banding fluids [38,39].

curve in Fig. 4(a) in terms of three structural regimes as captured by the structure parameter, λ, predicted by the TEVP model (see schematics in Fig. 4(b)). (*i*) In the low shear rate regime, $\dot{\gamma} \leqslant 0.1\ s^{-1}$, the nematic domains coexist in a percolating network which give rise to a solid-like response and plastic flow. Therefore, the structure parameter, λ, attains a value close to unity. (*ii*) At intermediate shear rates (shear banding regime, $0.1 < \dot{\gamma} < 100\ s^{-1}$), depicted by the grey area in Fig. 4, the integrity of the nematic domains is preserved whilst the breakage of the CNC network occurs to a different extent within the velocity gradient [19]. Remarkably, the stress overshoot in the shear-banding regime at $\dot{\gamma} \simeq 0.4\ s^{-1}$ is in close agreement with the thermal binding-unbinding rate of the physically cross-linked network junctions as obtained from the frequency sweep measurement (see arrow in Fig. 3(c)). In this range of imposed shear rates, the structure parameter λ exhibits a sharp decrease due to the collapse of the network. This sharp decrease in λ, causes a dramatic decrease of the thixotropic viscosity ($\eta_t = \eta_p \lambda^m$), and thus, a non-monotonic flow curve is predicted, leading to shear banding effects. (*iii*) In the high shear rate regime, $\dot{\gamma} > 100\ s^{-1}$, both the nematic domains and the network break into individual CNC rods, which align with the flow and give rise to a less pronounced shear-thinning state with reduced values of the shear viscosity (illustrated by the greater slope of τ_{xy} for $\dot{\gamma} > 100\ s^{-1}$ in Fig. 4(a)). Mirroring the completely destructured state of the material, λ reaches a plateau value λ_∞ at high shear rates. Since no further structural rearrangements are possible, a viscous fluid-like behaviour is predicted as $\dot{\gamma} \to \infty$.

In Fig. 4(c) we plot the predicted first normal stress difference (N_1) versus the imposed shear rate $\dot{\gamma}$. Note that we present only the predictions of the model; special experimental protocols are necessary for obtaining consistent measurements of N_1 in yield stress fluids [51], something that is outside the scope of the present study. First of all, we observe that N_1 is qualitatively similar to the shear stress flow curve (Fig. 4(a)), but for all the spectrum of shear rates that we examined, N_1 attains lower values than the respective value of the shear stress ($N_1 \sim 0.1\tau_{xy}$). This observation is clearly associated with the relatively low extensibility of the deforming CNC network. Additionally, a normal stress plateau is predicted in the low shear rate regime, which has been experimentally observed in gels and emulsions [51]. This plateau expresses the elasto-plastic response of the material (its ability to recover part of the imposed deformation when exposed to very low shear rates), and its value is inversely proportional to the elastic modulus (G) of the material. In the shear banding and high shear rate regimes, N_1 exhibits non-monotonic behaviour with increasing shear rates, resembling those observed in wormlike micellar solutions [52]. Such similarity is conceivable because of the physical breakage and reforming phenomena that govern the rheological response in both types of fluid.

Summarizing this section, the TEVP model is able to accurately reproduce the shear response of the SG over a broad range of shear rates. The shear stress plateau in the plastic regime, as well as the onset of shear banding from the rheological measurements, are captured very well by the model. Moreover, the TEVP model provides a microstructural parameter λ that appropriately describes the rearrangements of the CNC structure with the imposed shear rate.

4.1.3. Uniaxial elongation

To obtain insights into the extensional properties of the SG, we used the capillary breakup extensional rheometer (CaBER) [53]. The SG displayed a similar thinning profile as water (ESI, Fig. S3), i.e., the lack of an "elasto-capillary" regime associated with strong extension hardening resisting the rupture of the liquid bridge. This observation is consistent with Lundahl et al.'s report of an aqueous suspension of cellulose nanofibrils [54]. The lack of the "elasto-capillary" regime in the CaBER experiment impedes any experimental estimation of the uniaxial extensional viscosity. Therefore,

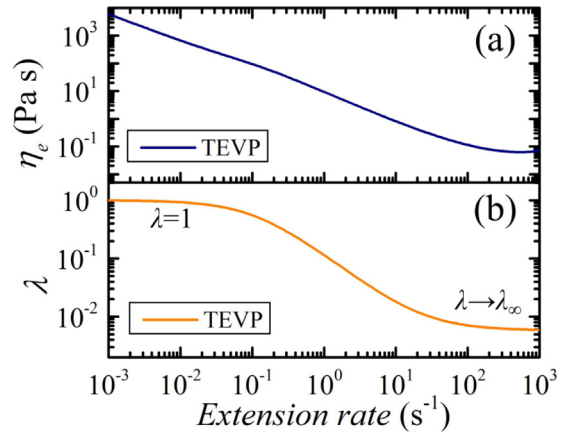

Fig. 5. (a) Steady extensional viscosity and (b) steady structure parameter versus extension rate in uniaxial elongation, as obtained from the TEVP model for the SG.

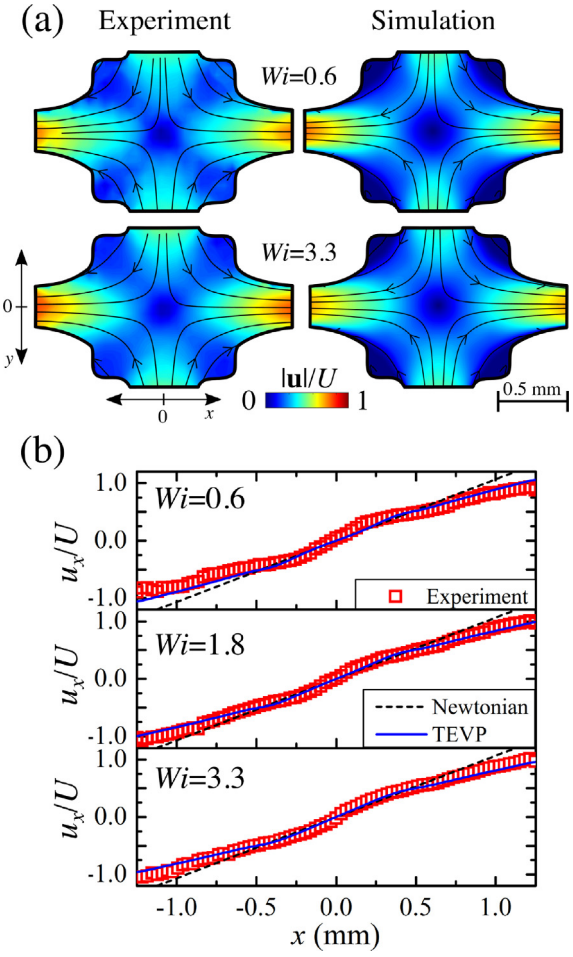

Fig. 6. (a) Normalized velocity fields $|\mathbf{u}|/U$ with superimposed streamlines for the flow of the SG in the OSCER at different values of *Wi*. The left column shows experimental data obtained by PIV, while the right column shows simulation results by using the TEVP model. The streamlines are determined by integration of the respective velocity field. (b) Normalized velocity u_x/U at the plane $y = 0$ mm as a function of the *x*-coordinate of the OSCER for the SG. Experimental data (symbols) are compared with the prediction of the TEVP model (blue line) for three values of *Wi*. The black dashed line is the expected velocity profile for a Newtonian fluid.

we employed the TEVP model to predict the steady uniaxial extensional viscosity $\eta_e = (\tau_{xx} - \tau_{yy})/\dot{\varepsilon}$, as a function of the extension rate, $\dot{\varepsilon}$ (Fig. 5(a)). The model predicts a strong extensional thinning trend which can be rationalized by the rigid rod-like nature of the CNC. The nearly inextensible rods do not exhibit extensional hardening, but their orientation in the extensional flow favours sliding between the rods, promoting the breakdown of the network and nematic domains [54]. At high extension rates ($\dot{\varepsilon} > 400\ s^{-1}$), the extensional viscosity reaches a plateau. This extensional viscosity response is related to the fully decomposed SG structure as given by the structural parameter $\lambda \to \lambda_\infty$ (Fig. 5(b)), leading to a dominant viscous behaviour. Thus the predictions of the model in elongation are consistent with the observed absence of an elastic resistance in the CaBER experiments.

4.1.4. Planar elongation

The OSCER device is designed to generate pure planar elongational flow in a large region around the stagnation point at the centre of the geometry in order to enable extensional rheometry [26]. It is therefore employed to probe the structural and mechanical properties of the SG under pure elongational deformations (shear-free) [27]. As we see in Fig. 6(a), experiments and 2D simulations display an overall good agreement in the flow field. The main features, such as the hyperbolic-like streamlines and the X-shaped pattern of low velocity magnitude near the stagnation point of the OSCER device, are well captured by the TEVP model.

To obtain a quantitative evaluation of flows at different *Wi*, the *x*-component of the velocity, u_x, along the elongational axis (*x*-axis) is plotted in Fig. 6(b). Both experimental and theoretical data show that u_x increases with *x*, however the curve deviates from the expected linear trend observed for a Newtonian fluid (dashed line) [22,26]. Specifically, the plots display two distinct linear trends. At $|x| < 0.4$ the velocity increases more rapidly than the Newtonian case, whilst the opposite trend is observed for $|x| > 0.4$. This characteristic two-step linear increase of $u_x$is quantitatively captured by the simulation for all the spectrum of *Wi* tested. Similar "bumps" in the distribution of u_x have been also reported for a Pluronic solution (non-thixotropic yield stress fluid) and are considered a fingerprint of the plasticity for materials flowing in the OSCER [43].

To get further insight about the connection between the mechanical and structural properties of the SG when exposed to elongational flow fields, we plot side by side the dimensionless principal stress difference, $PSD^* = PSD/(\eta_p U/H)$ where $PSD = \sqrt{(\tau_{xx} - \tau_{yy})^2 + 4\tau_{xy}^2}$, and the yielded surfaces obtained by the TEVP model, with the experimentally determined FIB (Fig. 7). The yield surfaces are obtained by setting the yield stress as the threshold value ($\tau_D = \tau_y$). According to the model, in the blue regions the material responds like an elastic solid, while in the red regions it behaves like a weakly viscoelastic fluid. Thus, we expect that in the blue regions, the elasticity originates from the percolating CNC network, whilst in the red regions, the viscous response arises from the breakage of the CNC network and the flow-induced CNC alignment. The FIB experiment probes the retardance intensity, δ, (displayed by the contour plot in Fig. 7(c)), which describes the extent of anisotropy within the system and scales with the volume fraction of the aligned particles, $\phi_{aligned}$ as $\delta \propto \phi_{aligned}$. Moreover, the FIB experiment provides information about the orientation of the slow optical axis, θ, directly probing the CNC orientation (see black segments in Fig. 7(c) for $Wi = 0.6$). The PSD^* and δ profiles show clear correlations as expected by the stress-optical law, stating that $PSD \propto \delta$ [55]. Specifically, the PSD^* fields display a maximum around the stagnation point and 4 localised stress minima further away, close to the salient corners of the OSCER (Fig. 7(a)). These stress minima correspond to the unyielded islands and to the area of low retardance in the FIB plots. Similar yield surfaces were recently reported in flows of ideal (non-thixotropic) yield-stress fluids in the OSCER device

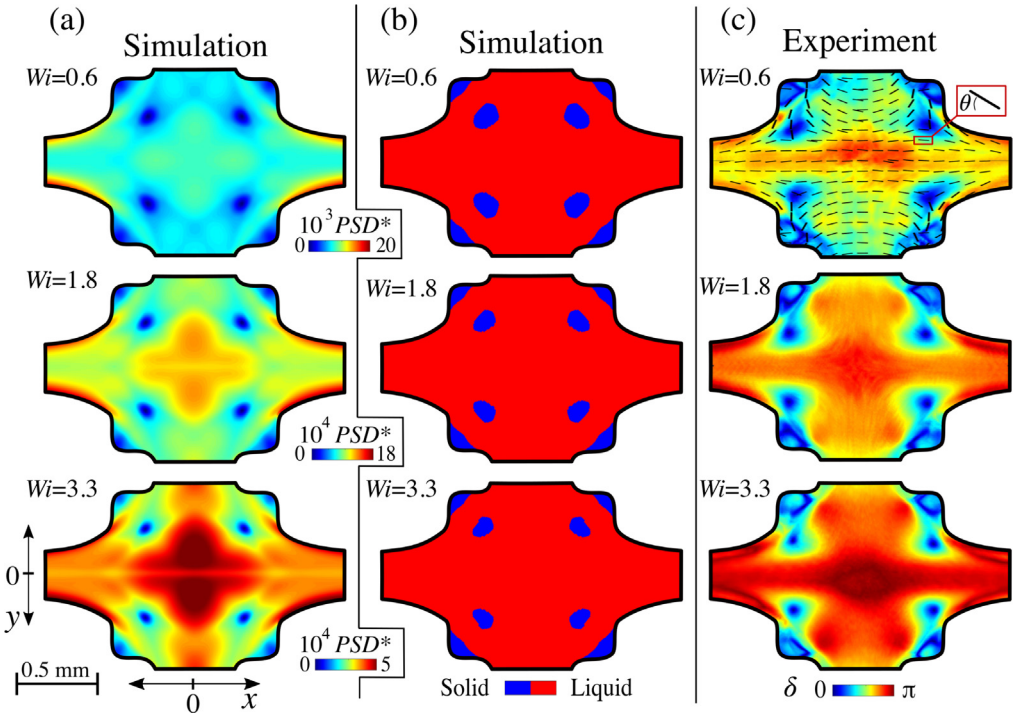

Fig. 7. (a) Distribution of PSD^* and (b) yield surfaces (blue: solid, red: fluid) as predicted by the simulation for the SG in the OSCER at different values of *Wi*. In (c) the corresponding FIB experiment with the retardance intensity (δ), indicated by the contour plot, and a representative direction of slow optical axis (θ), indicated by the short black segments (top panel).

[43]. Specifically, Varchanis et al. [43] found that the fluid elements entering the unyielded regions solidify and undergo solid body rotation prior to reliquefaction upon exiting the region. We note that the position of the unyielded regions in the experiment (areas of low birefringence) exhibit stronger asymmetry with respect to the $y = \pm x$ lines than the simulated ones, being located closer to the x-axis in the experiment. This is attributed to the fact that the TEVP model predicts a more rapid rebuild of the CNC network than what occurs in a real fluid. Nevertheless, as Wi is increased the match becomes progressively better. Also, with increasing Wi, the simulation predicts a reduced area of the unyielded regions due to the stress propagation further away from the stagnation point. The predicted reduction of the unyielded areas with increasing Wi is experimentally supported by the similar shrinkage of the areas comprising low retardance ($\delta \simeq \pi/4$) in the FIB plots. Note that the retardance pattern displayed in Fig. 7(c) substantially diverges from the reported case of a dilute, Newtonian-like, CNC suspension [22]. This suggests that the unyielded regions at the salient corners of the OSCER and those undergoing solid body rotation disturb the expected ideal extensional flow field [26,43], revealing the plastic properties of the SG. Analogously, the pronounced stress area around the stagnation point (the region of homogeneous extension rates) matches with the yielded portions of the yield surfaces and the strong retardance intensity in the FIB plots. The orientation of the slow optical axis (short black segments in the FIB plot, Fig. 7(c) at $Wi = 0.6$), indicates that the CNC orient parallel to the flow along the elongational axis and perpendicular to the flow along the compressional axis, as expected for colloidal rods in extensional flows [22]. This indicates that the material is in its liquid state above the value of the yield stress ($\tau_y = 3.9$ Pa), enabling the CNC to undergo flow-induced alignment and causing strong birefringence. The presence of solid-like regions within a fluidized matrix results from a complex interplay between structural breakage and reformation. In the areas of the OSCER geometry where the stress experienced by the fluid is below τ_y, the structural build-up wins over the structural breakage and the CNC assemble in a transient stress-bearing network (solid-like). In the areas of high stress, structural breakage outweighs structural build-up and the material liquefies (red liquid regions in Fig. 7(b)).

The simulation (Fig. 7(a)) also predicts a strand of lower stresses exactly on the x-axis passing through the stagnation point, which is related to the strong overshoots in the start-up extensional viscosity (see ESI, Fig. S4). The same pattern has been observed experimentally (through FIB) and predicted theoretically in simple cross-slot flows of long-chain branched polyethylenes [56], and was also attributed to overshoots in the start-up extensional viscosity. However, this phenomenon is not clearly visible in the FIB experiment for $Wi = 3.3$, suggesting that even though the SG exhibits overshoots in the start-up extensional viscosity the effect is weaker than what the TEVP model predicts (ESI Fig. S4).

4.2. Mixed flow

After investigating the material behaviour in shear and extensional flows, we now examine the case where a combination of both shearing and extensional deformations determine the mechanical and structural properties of the fluid. In analogy to the benchmark experiment of the flow around a sphere, we employ a microfluidic platform containing a low blockage ratio microfluidic cylinder. The flow past a cylinder generates strong compressional and extensional kinematics upstream and downstream the cylinder, respectively, with strong shearing flow around the sides of the cylinder. Fig. 8(a) displays representative steady flow fields as obtained from experiments and simulations. For the experimentally determined velocity profiles, the flow field is laterally symmetric (with respect to the x-axis), with fluid passing equally on either side of the cylinder. A uniform (plug-like) flow profile develops for $x > 0.5$ mm. However, the fore-aft symmetry is broken, and along the centreline a localised area of high velocity is present a few cylinder radii downstream of the cylinder. Such velocity overshoot (velocity increase followed by a decrease) is referred to as a "negative wake", and is in contrast to the common behaviour of polymeric and wormlike micellar solutions around cylinders [29–31]. Nevertheless, the negative wake has been observed in flows past a sphere or a bubble with viscoelastic solutions, such as xanthan gum [57], poly(acrylamide) solution [58–61], as well as with EVP materials, such as Carbopol gels [62–65]. The formation of the negative wake has been related to a pronounced elasticity of the fluid and found to be strongly connected with its extensional viscosity [66]. Supporting our observation, extensional thinning [66] and uniform flow conditions (plug-like) [67] have been found to promote the presence of the negative wake. In contrast, the negative wake is absent in flows of highly extensional hardening viscoelastic solutions [29–32,68] and non-shear-thinning elastic fluids with parabolic (Poiseuille) flow profiles [32].

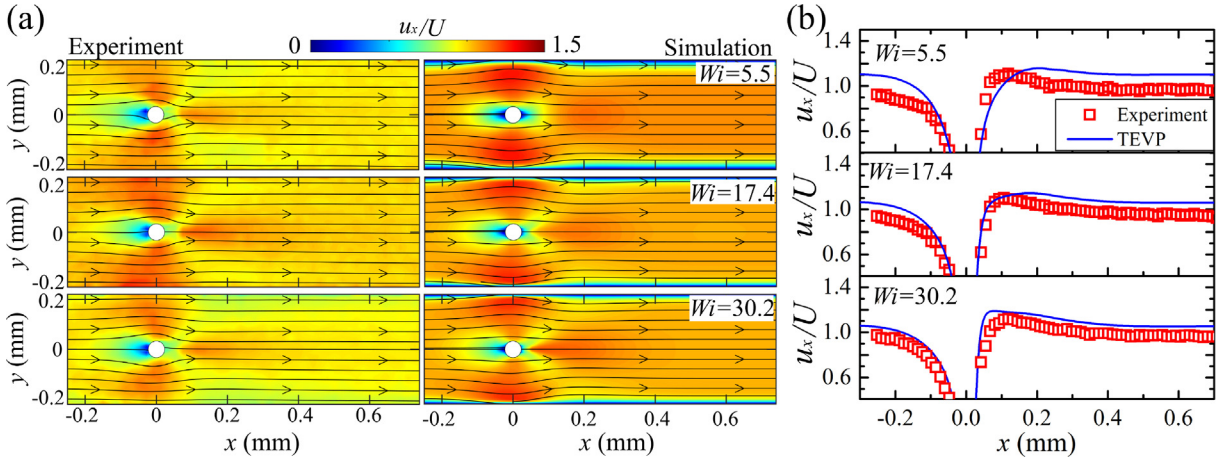

Fig. 8. (a) Normalized velocity fields u_x/U with superimposed streamlines for the flow of the SG in the MCD at different values of Wi. The left column shows experimental data obtained by PIV and the right column shows the simulations performed using the TEVP model. The streamlines are determined by integration of the respective velocity field. (b) Normalized velocity at the plane $y = 0$ mm as a function of the x-coordinate of the MCD for the SG. Experimental data (symbols) are compared with the prediction of the TEVP model (lines) for three values of Wi.

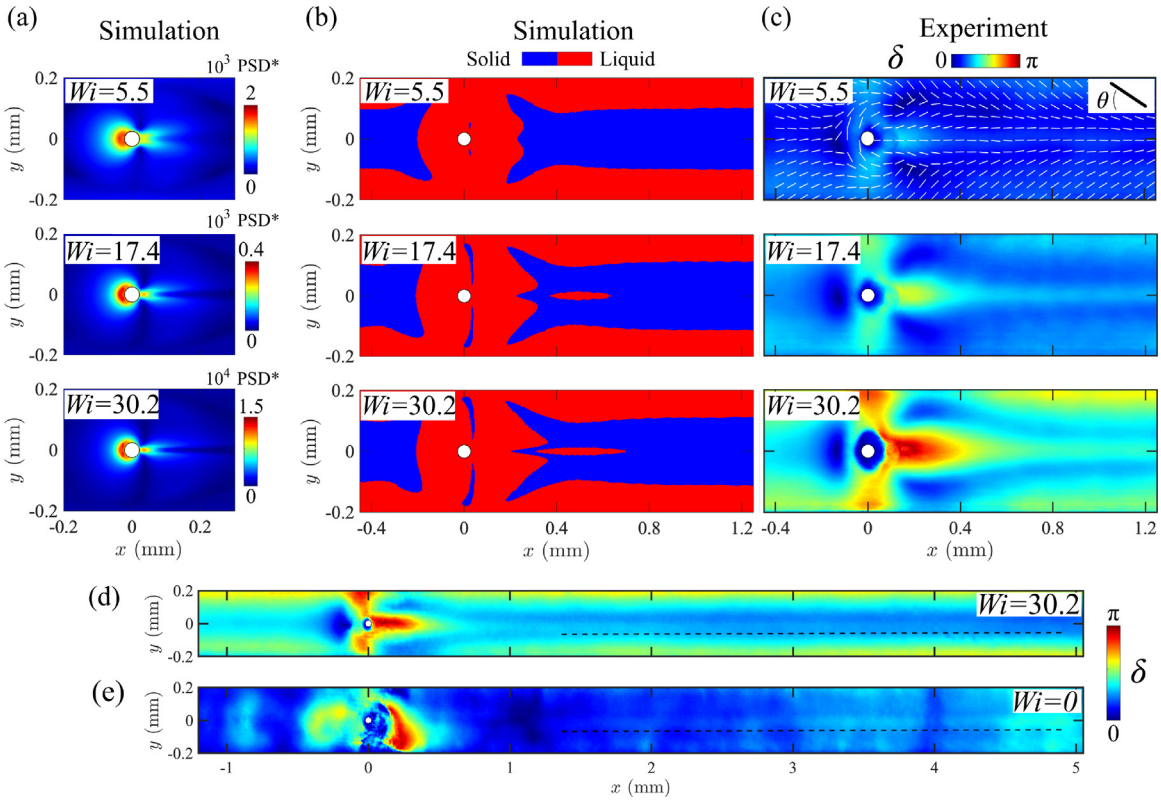

Fig. 9. (a) Distribution of PSD^* and (b) yield surfaces (blue: solid, red: fluid) as predicted by the simulation for the SG in the MCD at three values of Wi (rows). In (c) the corresponding FIB experiment with the retardance intensity (δ), indicated by the contour plot, and a representative direction of slow optical axis (θ), indicated by the white segments (top panel). FIB experiment at (d) $Wi = 30.2$ and (e) at rest ($Wi = 0$) approx 24 h after the flow stoppage (from $Wi = 30.2$). Horizontal dashed lines in (d) and (e) indicate the birefringent wake downstream of the cylinder.

Proceeding to a comparison of the experimental flow profiles with the simulated ones, we observe in Fig. 8(a) that the TEVP model can predict qualitatively all the characteristics of the velocity distribution, such as the negative wake, and the lateral symmetry of the flow (recent experiments [30,31] and simulations [32] also revealed laterally asymmetric flows in the same microcylinder geometry using viscoelastic and wormlike micellar solutions) and the V-shaped velocity distribution downstream of the rear pole of the cylinder. In addition, Fig. 8(b) presents a quantitative comparison of the velocity profiles along $y = 0$. Notably, the agreement between the experiments and the predictions of the TEVP model is very good for $5.5 \leqslant Wi \leqslant 30.2$ (Fig. 8(b)). At $Wi = 5.5$, where the flow is at the onset of the shear banding regime, the predicted velocity overshoot is slightly shifted downstream compared to the experimental observation, whilst the velocity downstream the cylinder, where the plug-like flow has been established, is predicted slightly higher by the model ($\sim 10\%$). For $Wi = 17.4$ and 30.2, which are both in the shear-banding regime, we observe that the model can predict both the magnitude and the location of the negative wake, as well as the value of the velocity downstream of the cylinder with very good accuracy. At high Wi the flow recovers the fore-aft symmetry, as shown experimentally for $Wi = 406$ (see ESI, Fig. S5(a)). However, at $Wi = 406$ the TEVP model still predicts the negative wake (see ESI, Fig. S5(b)) and the loss of the negative wake is reached only at much higher values of Wi (e.g., $Wi = 6300$, see ESI Fig. S5(b-c)). Accordingly, at high $Wi > 30.2$, predictions of the TEVP model are only qualitative.

Using the results from the simulations for $Wi \leqslant 30.2$, we computed the normalized principal stress difference, PSD^* (Fig. 9(a)). The stress is fore-aft asymmetric with a V-shaped area of pronounced stress downstream of the cylinder. A similar V-shaped area of low velocity is also visible in the velocity profiles (Fig. 8(a)), analogous to the V-shaped low velocity patterns reported for bubbles rising in an elastic shear thinning fluid [69,70]. Varchanis et al. [32] showed that for a non-elastic but shear thinning fluid flowing in the same microfluidic geometry as that used in the present work, the fore-aft symmetry of the PSD^* profiles is maintained. Contrarily, elastic fluids with extension hardening properties exhibited for-aft asymmetry of the PSD^* with a much longer downstream wake than the one displayed in Fig. 9(a) [32]. This V-shaped stress profile is again attributed to the intense overshoots in the startup extensional viscosity that the TEVP model predicts (see ESI for detailed explanation). We also observe a mismatch between the experimental δ and the predicted PSD_* profiles along each side of the cylinder. As we can clearly observe in Fig. 9(c) for $Wi = 30.2$, strong alignment takes place at those regions due to the pronounced stress, something that is not predicted by the model (Fig. 9(a)). This can be related to the fact that the model predicts excessive strain thinning effects, and thus, a more plug-like velocity profile at the sides of the cylinder. This leads to the prediction of localized stresses only in close proximity to the cylinder.

To gain further insights regarding the origin of the negative wake, we examine the yield surfaces predicted by the TEVP model (Fig. 9(b)). The yield surfaces indicate that the SG in the proximity of the walls and around the cylinder is in a liquid state as it experiences greater stresses than the yield stress. Note that the negative wake occurs within the liquid portion of the fluid, suggesting that a pronounced elasticity by itself is not essential for the development of the negative wake. However, increasing Wi beyond $Wi \sim 30.2$, liquefies the SG, with its velocity fields gaining fore-aft symmetry for $Wi = 406$ (see ESI Fig. S5). This observation can be explained by the fact that at high flow rates, the SG breaks down completely, and the lower plateaus in shear and extensional viscosity are reached. Consequently, the material behaves as a Newtonian-like

fluid, and the negative wake vanishes. This suggests that a relative balance between elastic and viscous effects is necessary to induce the negative wake, and that when one of them dominates over the other the phenomenon is precluded.

By comparing the simulated yield surfaces Fig. 9(b) with the experimentally determined FIB in Fig. 9(c) it is possible to obtain a comprehensive understanding of the interplay between the mechanical properties of the SG and the structural organization of the CNC under flow. The yielded regions shown in red (Fig. 9 (b)) broadly correspond to the high intensity regions of δ (Fig. 9 (c)). This is especially evident near the walls and a few radii downstream of the cylinder where a pronounced retardance intensity is present. Therefore, it appears that the extent of the CNC alignment is greater when the SG is in the liquid state, as previously proposed by Hausmann et al. [71] for repulsive CNC glasses. As indicated by the orientation of the slow optical axis (see solid segments in Fig. 9 (c) for $Wi = 5.5$)), the CNC aligns parallel to the flow in the zones of strong elongational flow (e.g., downstream of the cylinder) and tend to a perpendicular orientation to the flow in the zones of strong compressional flow (e.g., upstream of the cylinder). From a structural perspective, it is plausible to hypothesise that the negative wake (velocity overshoot in Fig. 8) originates from the pronounced parallel alignment of the CNC in the wake of the cylinder. However, this hypothesis is not corroborated by the persistence of the CNC alignment with the loss of the negative wake for high values of *Wi*. On the contrary, the negative wake seems to occur when structural build-up and structural breakage are both at play, thus, only when the CNC aligns in the yielded (liquid) portion around the cylinder and a stress-bearing network (solid) forms far downstream of the cylinder (Fig. 9(b)). The TEVP model predicts a structural build-up along the centreline far downstream of the cylinder ($y = 0$ mm for $x > 0.3$ mm) which is supported by the persisting δ wake extending up to $x \approx 5$ mm even approx 24h after the flow stoppage (from $Wi = 30.2$ to $Wi = 0$, see dashed lines in Fig. 9(d,e)). This indicates that in the proximity of the cylinder, a fraction of the CNC ($\phi_{aligned}$) aligns with the flow and further downstream the stress decreases to values below the yield stress of the material, allowing the structural build-up of the CNC network. As such, the network formation causes caging of the $\phi_{aligned}$ CNC, hindering their relaxation towards isotropy even in the absence of flow (Fig. 9(e)). By contrast, upon flow stoppage, the yielded fluid in proximity of the cylinder enables a prompt Brownian-dominated reorganization of the CNC towards a favourable configuration. We note that the birefringence pattern in proximity of the cylinder for the SG at rest (Fig. 9(e)) must be regarded indicatively due to secondary effects appearing upon flow stoppage (e.g., dissipation of the elastic energy within the SG).

5. Summary and conclusions

We have investigated the mechanical and structural properties of a structurally ordered soft glass (SG) composed of rigid, rod-like cellulose nanocrystals (CNC), in simple and mixed flows. The SG is modeled with a thixotropic elasto-visco-plastic (TEVP) constitutive model that predicts all the characteristic rheological features corresponding to important structural changes in the sample. By characterizing the material in simple and oscillatory shear, we find that its rheological properties strongly depend on the imposed deformation rate and can be well captured by the TEVP model. For small deformation rates, the microstructure is fully assembled in a bi-phasic structure composed of nematic domains embedded within a percolating network and the structure parameter $\lambda \sim 1$. This leads to solid-like response and plastic flow. At greater flow rates, the breakage of the CNC network is manifested by the dramatic decrease in λ, leading to a non-monotonic flow curve with pronounced shear banding effects. With further increasing flow rates, the nematic domains are also destroyed, thus, $\lambda \to \lambda_\infty$ and the material behaves like a Newtonian fluid. In uniaxial extension, the TEVP model predicts an intense extension-rate-thinning behaviour originating from the rapid microstructural breakdown and supported by the absence of an elasto-capillary regime in capillary thinning experiments. In planar extension generated by the OSCER, the experiments and simulations revealed the presence of large unyielded islands and a two-step velocity gradient around the stagnation point, verifying the plastic nature of the material. To investigate the case of mixed kinematics, the sample was driven through a microchannel featuring a rigid microcylinder and the structure-property interplay was experimentally analysed using micro-particle image velocimetry and flow induced birefringence techniques. The most remarkable observation was the development of a velocity overshoot (negative wake) downstream the cylinder, which was also well captured by the model. The negative wake was observed only within a range of *Wi*, which enabled the coexistence of yielded (viscous-dominated) and unyielded (elastic-dominated) regions around the microcylinder. As the SG entered a fully fluidized state at high *Wi*, corresponding to the high-shear rate regime in the flow curve, the negative wake vanished, and the flow gained fore-aft symmetry. The simulations based on the TEVP model predicted quantitatively the experimental flow fields up to values of $Wi \approx 30$ and captured the structural fingerprint of the material with good accuracy.

Previous studies have focused on the structural-property relationship of rod-like cellulose nanoparticles in shearing [22,72,73], extensional flows [22], and expansion-contraction geometries [71,74–76]. However, effects of mixed flows generated by obstacles along the flow path on inducing structural and rheological changes of cellulose-based suspensions have not been explored. Our study demonstrates that mixed flow conditions can be utilized as a straightforward methodology to achieve ordered colloidal assembly. Specifically, we show that the flow around an obstacle (i.e., cylindrical shape in this study) is a simple and accessible way to achieve mixed flow conditions and induce anisotropic assembly. To advance this concept further, the role of the size and shape of the obstacle needs to be determined in future studies. We expect that our results are extendable to other rod-like colloidal suspensions (e.g., amyloid fibrils and viruses) provided that analogous rheological features as those reported herein are met. The comprehensive understanding advanced in this study opens new avenues for tailoring directional assembly in soft materials where tunability is key to utility.

CRediT authorship contribution statement

Vincenzo Calabrese: Conceptualization, Investigation, Methodology, Data curation, Validation, Writing - original draft. **Stylianos Varchanis:** Investigation, Methodology, Data curation, Validation, Writing - original draft, Software. **Simon J. Haward:** Supervision, Resources, Writing - review & editing. **John Tsamopoulos:** Supervision, Resources, Writing - review & editing. **Amy Q. Shen:** Supervision, Resources, Funding acquisition, Writing - review & editing.

Declaration of Competing Interest

The authors declare that they have no known competing financial interests or personal relationships that could have appeared to influence the work reported in this paper.

Acknowledgements

The authors gratefully acknowledge the support of Okinawa Institute of Science and Technology Graduate University with

subsidy funding from the Cabinet Office, Government of Japan. S.J.H. and A.Q.S. also acknowledge financial support from the Japanese Society for the Promotion of Science (JSPS, Grant Nos. 18K03958, 18H01135, and 21K03884) and the Joint Research Projects (JRPs) supported by the JSPS and the Swiss National Science Foundation (SNSF). J.T. also acknowledge financial support from the Hellenic Foundation of Research and Innovation (HFRI, Grant No. FM17-2309).

Appendix A. Supplementary material

Supplementary data associated with this article can be found, in the online version, at https://doi.org/10.1016/j.jcis.2021.05.103.

References

[1] M.J. Solomon, P.T. Spicer, Microstructural regimes of colloidal rod suspensions, gels, and glasses, Soft Matter 6 (7) (2010) 1391–1400, https://doi.org/10.1039/b918281k.
[2] M. Doi, S.F. Edwards, Dilute solutions of rigid rodlike polymers, in: The Theory of Polymer Dynamics, 1986, pp. 289–323.
[3] Y. Xu, A.D. Atrens, J.R. Stokes, "Liquid, gel and soft glass" phase transitions and rheology of nanocrystalline cellulose suspensions as a function of concentration and salinity, Soft Matter 14 (10) (2018) 1953–1963, https://doi.org/10.1039/C7SM02470C.
[4] M. Doi, S.F. Edwards, Semidilute solutions of rigid rodlike polymers, in: The Theory of Polymer Dynamics, 1986, pp. 324–348.
[5] C. Lang, J. Kohlbrecher, L. Porcar, A. Radulescu, K. Sellinghoff, J.K.G. Dhont, M.P. Lettinga, Microstructural understanding of the length- and stiffness-dependent shear thinning in semidilute colloidal rods, Macromolecules 52 (24) (2019) 9604–9612, https://doi.org/10.1021/acs.macromol.9b01592.
[6] M. Doi, S.F. Edwards, Concentrated solutions of rigid rodlike polymers, in: The Theory of Polymer Dynamics, 1986, pp. 350–379.
[7] J. Schmitt, V. Calabrese, M.A. Da Silva, S. Lindhoud, V. Alfredsson, J.L. Scott, K.J. Edler, TEMPO-oxidised cellulose nanofibrils: Probing the mechanisms of gelation via small angle X-ray scattering, Phys. Chem. Chem. Phys. 20 (23) (2018) 16012–16020, https://doi.org/10.1039/c8cp00355f.
[8] H. Fukuzumi, R. Tanaka, T. Saito, A. Isogai, Dispersion stability and aggregation behavior of TEMPO-oxidized cellulose nanofibrils in water as a function of salt addition, Cellulose 21 (3) (2014) 1553–1559, https://doi.org/10.1007/s10570-014-0180-z.
[9] D. Bonn, H. Kellay, H. Tanaka, G. Wegdam, J. Meunier, Laponite: What is the difference between a gel and a glass?, Langmuir 15 (22) (1999) 7534–7536, https://doi.org/10.1021/la990167+.
[10] M. Nordenström, A. Fall, G. Nyström, L. Wågberg, Formation of colloidal nanocellulose glasses and gels, Langmuir 33 (38) (2017) 9772–9780, https://doi.org/10.1021/acs.langmuir.7b01832.
[11] V. Calabrese, J.C. Muñoz-García, J. Schmitt, M.A. da Silva, J.L. Scott, J. Angulo, Y. Z. Khimyak, K.J. Edler, Understanding heat driven gelation of anionic cellulose nanofibrils: Combining saturation transfer difference (STD) NMR, small angle X-ray scattering (SAXS) and rheology, J. Colloid Interface Sci. 535 (2019) 205–213, https://doi.org/10.1016/j.jcis.2018.09.085.
[12] H. Hasegawa, Y. Horikawa, T. Shikata, Cellulose nanocrystals as a model substance for rigid rod particle suspension rheology, Macromolecules 53 (7) (2020) 2677–2685, https://doi.org/10.1021/acs.macromol.9b02641.
[13] M.S. Reid, M. Villalobos, E.D. Cranston, Benchmarking cellulose nanocrystals: From the laboratory to industrial production, Langmuir 33 (7) (2017) 1583–1598, https://doi.org/10.1021/acs.langmuir.6b03765.
[14] E.E. Ureña-Benavides, G. Ao, V.A. Davis, C.L. Kitchens, Rheology and phase behavior of lyotropic cellulose nanocrystal suspensions, Macromolecules 44 (22) (2011) 8990–8998, https://doi.org/10.1021/ma201649f.
[15] P. Bertsch, S. Isabettini, P. Fischer, Ion-induced hydrogel formation and nematic ordering of nanocrystalline cellulose suspensions, Biomacromolecules 18 (12) (2017) 4060–4066, https://doi.org/10.1021/acs.biomac.7b01119.
[16] P. Bertsch, A. Sánchez-Ferrer, M. Bagnani, S. Isabettini, J. Kohlbrecher, R. Mezzenga, P. Fischer, Ion-induced formation of nanocrystalline cellulose colloidal glasses containing nematic domains, Langmuir 35 (11) (2019) 4117–4124, https://doi.org/10.1021/acs.langmuir.9b00281.
[17] Y. Xu, A. Atrens, J.R. Stokes, A review of nanocrystalline cellulose suspensions: Rheology, liquid crystal ordering and colloidal phase behaviour, Adv. Colloid Interface Sci. 275 (2020) 102076, https://doi.org/10.1016/j.cis.2019.102076.
[18] Y. Xu, A. Atrens, J.R. Stokes, Structure and rheology of liquid crystal hydroglass formed in aqueous nanocrystalline cellulose suspensions, J. Colloid Interface Sci. 555 (2019) 702–713, https://doi.org/10.1016/j.jcis.2019.08.022.
[19] Y. Xu, A.D. Atrens, J.R. Stokes, Liquid crystal hydroglass formed via phase separation of nanocellulose colloidal rods, Soft Matter 15 (8) (2019) 1716–1720, https://doi.org/10.1039/C8SM02288G.
[20] A. Hirai, O. Inui, F. Horii, M. Tsuji, Phase separation behavior in aqueous suspensions of bacterial cellulose nanocrystals prepared by sulfuric acid treatment, Langmuir 25 (1) (2009) 497–502, https://doi.org/10.1021/la802947m.
[21] C. Honorato-Rios, C. Lehr, C. Schütz, R. Sanctuary, M.A. Osipov, J. Baller, J.P.F. Lagerwall, Fractionation of cellulose nanocrystals: enhancing liquid crystal ordering without promoting gelation, NPG Asia Mater. (5) 455–465. doi: 10.1038/s41427-018-0046-1.
[22] V. Calabrese, S.J. Haward, A.Q. Shen, Effects of shearing and extensional flows on the alignment of colloidal rods, Macromolecules 54 (9) (2021) 4176–4185, https://doi.org/10.1021/acs.macromol.0c02155.
[23] R. Wagner, A. Raman, R.J. Moon, Transverse elasticity of cellulose nanocrystals via atomic force microscopy, in: 10th International Conference on Wood & Biofiber Plastic Composites, pp. 309–316. doi:10.1021/la903111j.
[24] S.L. Anna, G.H. McKinley, Elasto-capillary thinning and breakup of model elastic liquids, J. Rheol. 45 (1) (2001) 115–138, https://doi.org/10.1122/1.1332389.
[25] S.J. Haward, Microfluidic extensional rheometry using stagnation point flow, Biomicrofluidics 10 (4) (2016) 043401, https://doi.org/10.1063/1.4945604.
[26] S.J. Haward, M.S.N. Oliveira, M.A. Alves, G.H. McKinley, Optimized cross-Slot flow geometry for microfluidic extensional rheometry, Phys. Rev. Lett. 109 (12) (2012) 128301, https://doi.org/10.1103/PhysRevLett.109.128301.
[27] S.J. Haward, G.H. McKinley, A.Q. Shen, Elastic instabilities in planar elongational flow of monodisperse polymer solutions, Sci. Rep. 6 (1) (2016) 33029, https://doi.org/10.1038/srep33029.
[28] N. Burshtein, S.T. Chan, K. Toda-Peters, A.Q. Shen, S.J. Haward, 3D-printed glass microfluidics for fluid dynamics and rheology, Curr. Opin. Colloid Interface Sci. 43 (2019) 1–14, https://doi.org/10.1016/j.cocis.2018.12.005.
[29] S.J. Haward, K. Toda-Peters, A.Q. Shen, Steady viscoelastic flow around high-aspect-ratio, low-blockage-ratio microfluidic cylinders, J. Non-Newton. Fluid Mech. 254 (2018) 23–35, https://doi.org/10.1016/j.jnnfm.2018.02.009.
[30] S.J. Haward, N. Kitajima, K. Toda-Peters, T. Takahashi, A.Q. Shen, Flow of wormlike micellar solutions around microfluidic cylinders with high aspect ratio and low blockage ratio, Soft Matter 15 (9) (2019) 1927–1941, https://doi.org/10.1039/c8sm02099j.
[31] S.J. Haward, C.C. Hopkins, A.Q. Shen, Asymmetric flow of polymer solutions around microfluidic cylinders: Interaction between shear-thinning and viscoelasticity, J. Non-Newton. Fluid Mech. 278 (2020) 104250, https://doi.org/10.1016/j.jnnfm.2020.104250.
[32] S. Varchanis, C.C. Hopkins, A.Q. Shen, J. Tsamopoulos, S.J. Haward, Asymmetric flows of complex fluids past confined cylinders: A comprehensive numerical study with experimental validation, Phys. Fluids 32 (5) (2020) 053103, https://doi.org/10.1063/5.0008783.
[33] C.D. Meinhart, S. Wereley, M. Gray, Volume illumination for two-dimensional particle image velocimetry, Meas. Sci. Technol. 11 (6) (2000) 809–814, https://doi.org/10.1088/0957-0233/11/6/326.
[34] T.C. Papanastasiou, N. Malamataris, K. Ellwood, A new outflow boundary condition, Int. J. Numer. Meth. Fluids 14 (5) (1992) 587–608, https://doi.org/10.1002/fld.1650140506.
[35] S. Varchanis, G. Makrigiorgos, P. Moschopoulos, Y. Dimakopoulos, J. Tsamopoulos, Modeling the rheology of thixotropic elasto-visco-plastic materials, J. Rheol. 63 (4) (2019) 609–639, https://doi.org/10.1122/1.5049136.
[36] P. Saramito, A new constitutive equation for elastoviscoplastic fluid flows, J. Non-Newton. Fluid Mech. 145 (1) (2007) 1–14, https://doi.org/10.1016/j.jnnfm.2007.04.004.
[37] C.J. Dimitriou, G.H. McKinley, A comprehensive constitutive law for waxy crude oil: a thixotropic yield stress fluid, Soft Matter 10 (35) (2014) 6619–6644, https://doi.org/10.1039/C4SM00578C.
[38] S.M. Fielding, Complex dynamics of shear banded flows, Soft Matter 3 (2007) 1262–1279, https://doi.org/10.1039/B707980J.
[39] S. Lerouge, P.D. Olmsted, Non-local effects in shear banding of polymeric flows, Frontiers in Physics 7 (2020) 246, https://doi.org/10.3389/fphy.2019.00246.
[40] R.G. Larson, Y. Wei, A review of thixotropy and its rheological modeling, J. Rheol. 63 (3) (2019) 477–501, https://doi.org/10.1122/1.5055031.
[41] N.P. Thien, R.I. Tanner, A new constitutive equation derived from network theory, J. Non-Newton. Fluid Mech. 2 (4) (1977) 353–365, https://doi.org/10.1016/0377-0257(77)80021-9.
[42] C.-Y.D. Lu, P.D. Olmsted, R.C. Ball, Effects of nonlocal stress on the determination of shear banding flow, Phys. Rev. Lett. 84 (2000) 642–645, https://doi.org/10.1103/PhysRevLett.84.642.
[43] S. Varchanis, S.J. Haward, C.C. Hopkins, A. Syrakos, A.Q. Shen, Y. Dimakopoulos, J. Tsamopoulos, Transition between solid and liquid state of yield-stress fluids under purely extensional deformations, Proc. Natl. Acad. Sci. USA 117 (23) (2020) 12611–12617. doi: 10.1073/pnas.1922242117.
[44] S. Varchanis, Y. Dimakopoulos, J. Tsamopoulos, Evaluation of tube models for linear entangled polymers in simple and complex flows, J. Rheol. 62 (1) (2018) 25–47, https://doi.org/10.1122/1.5009197.
[45] S. Varchanis, A. Syrakos, Y. Dimakopoulos, J. Tsamopoulos, A new finite element formulation for viscoelastic flows: Circumventing simultaneously the LBB condition and the high-Weissenberg number problem, J. Non-Newton. Fluid Mech. 267 (2019) 78–97, https://doi.org/10.1016/j.jnnfm.2019.04.003.
[46] S. Varchanis, A. Syrakos, Y. Dimakopoulos, J. Tsamopoulos, PEGAFEM-V: A new Petrov-Galerkin finite element method for free surface viscoelastic flows, J. Non-Newton. Fluid Mech. 284 (2020) 104365, https://doi.org/10.1016/j.jnnfm.2020.104365.
[47] V. Calabrese, M.A. da Silva, L. Porcar, S.J. Bryant, K.M.Z. Hossain, J.L. Scott, K.J. Edler, Filler size effect in an attractive fibrillated network: a structural and rheological perspective, Soft Matter 16 (13) (2020) 3303–3310, https://doi.org/10.1039/C9SM02175B.

[48] K. Hyun, S.H. Kim, K.H. Ahn, S.J. Lee, Large amplitude oscillatory shear as a way to classify the complex fluids, J. Non-Newton. Fluid Mech. 107 (1–3) (2002) 51–65, https://doi.org/10.1016/S0377-0257(02)00141-6.
[49] G.J. Donley, P.K. Singh, A. Shetty, S.A. Rogers, Elucidating the "G" overshoot in soft materials with a yield transition via a time-resolved experimental strain decomposition, Proc. Natl. Acad. Sci. USA 117(36) (2020) 21945–21952. doi: 10.1073/pnas.2003869117.
[50] O. Lieleg, M.M.A.E. Claessens, Y. Luan, A.R. Bausch, Transient binding and dissipation in cross-Linked actin networks, Phys. Rev. Lett. 101 (10) (2008) 108101, https://doi.org/10.1103/PhysRevLett.101.108101.
[51] H. de Cagny, M. Fazilati, M. Habibi, M.M. Denn, D. Bonn, The yield normal stress, J. Rheol. 63 (2) (2019) 285–290, https://doi.org/10.1122/1.5063796.
[52] N. Germann, A. Kate Gurnon, L. Zhou, L. Pamela Cook, A.N. Beris, N.J. Wagner, Validation of constitutive modeling of shear banding, threadlike wormlike micellar fluids, J. Rheol. 60(5) (2016) 983–999. doi: 10.1122/1.4959292.
[53] S.L. Anna, G.H. McKinley, D.A. Nguyen, T. Sridhar, S.J. Muller, J. Huang, D.F. James, An interlaboratory comparison of measurements from filament-stretching rheometers using common test fluids, J. Rheol. 45 (1) (2001) 83–114, https://doi.org/10.1122/1.1332388.
[54] M.J. Lundahl, M. Berta, M. Ago, M. Stading, O.J. Rojas, Shear and extensional rheology of aqueous suspensions of cellulose nanofibrils for biopolymer-assisted filament spinning, Eur. Polym. J. 109 (2018) 367–378, https://doi.org/10.1016/j.eurpolymj.2018.10.006.
[55] T.J. Ober, J. Soulages, G.H. McKinley, Spatially resolved quantitative rheo-optics of complex fluids in a microfluidic device, J. Rheol. 55 (5) (2011) 1127–1159, https://doi.org/10.1122/1.3606593.
[56] D.M. Hoyle, Q. Huang, D. Auhl, D. Hassell, H.K. Rasmussen, A.L. Skov, O.G. Harlen, O. Hassager, T.C.B. McLeish, Transient overshoot extensional rheology of long-chain branched polyethylenes: Experimental and numerical comparisons between filament stretching and cross-slot flow, J. Rheol. 57 (1) (2013) 293–313, https://doi.org/10.1122/1.4767982.
[57] M.M. Mrokowska, A. Krztoń-Maziopa, Viscoelastic and shear-thinning effects of aqueous exopolymer solution on disk and sphere settling, Sci. Rep. 9 (1) (2019) 1–13, https://doi.org/10.1038/s41598-019-44233-z.
[58] M.T. Arigo, G.H. McKinley, An experimental investigation of negative wakes behind spheres settling in a shear-thinning viscoelastic fluid, Rheol. Acta 37 (4) (1998) 307–327, https://doi.org/10.1007/s003970050118.
[59] O. Hassager, Negative wake behind bubbles in non-Newtonian liquids, Nature 279 (5712) (1979) 402–403, https://doi.org/10.1038/279402a0.
[60] C. Bisgaard, Velocity fields around spheres and bubbles investigated by laser-Doppler anemometry, J. Non-Newton. Fluid Mech. 12 (3) (1983) 283–302, https://doi.org/10.1016/0377-0257(83)85003-4.
[61] D. Fraggedakis, M. Pavlidis, Y. Dimakopoulos, J. Tsamopoulos, On the velocity discontinuity at a critical volume of a bubble rising in a viscoelastic fluid, J. Fluid Mech. 789 (2016) 310–346, https://doi.org/10.1017/jfm.2015.740.
[62] Y. Holenberg, O.M. Lavrenteva, U. Shavit, A. Nir, Particle tracking velocimetry and particle image velocimetry study of the slow motion of rough and smooth solid spheres in a yield-stress fluid, Phys. Rev. E 86 (2012) 066301, https://doi.org/10.1103/PhysRevE.86.066301.
[63] D. Fraggedakis, Y. Dimakopoulos, J. Tsamopoulos, Yielding the yield-stress analysis: a study focused on the effects of elasticity on the settling of a single spherical particle in simple yield-stress fluids, Soft Matter 12 (2016) 5378–5401, https://doi.org/10.1039/C6SM00480F.
[64] D. Fraggedakis, Y. Dimakopoulos, J. Tsamopoulos, Yielding the yield stress analysis: A thorough comparison of recently proposed elasto-visco-plastic (EVP) fluid models, J. Non-Newton. Fluid Mech. 238 (2016) 170–188, https://doi.org/10.1016/j.jnnfm.2016.11.007.
[65] A.M.V. Putz, T.I. Burghelea, I.A. Frigaard, D.M. Martinez, Settling of an isolated spherical particle in a yield stress shear thinning fluid, Phys. Fluids 20 (3) (2008) 033102, https://doi.org/10.1063/1.2883937.
[66] H.S. Dou, N. Phan-Thien, Criteria of negative wake generation behind a cylinder, Rheol. Acta 43 (3) (2004) 203–209, https://doi.org/10.1007/s00397-003-0332-9.
[67] J.M. Kim, C. Kim, C. Chung, K.H. Ahn, S.J. Lee, Negative wake generation of FENE-CR fluids in uniform and Poiseuille flows past a cylinder, Rheol. Acta 44 (6) (2005) 600–613, https://doi.org/10.1007/s00397-005-0442-7.
[68] G.H. McKinley, R.C. Armstrong, R. Brown, The wake instability in viscoelastic flow past confined circular cylinders, Philos. Trans. Roy. Soc. Lond. Ser. A: Phys. Eng. Sci. 344 (1671) (1993) 265–304, https://doi.org/10.1098/rsta.1993.0091.
[69] D. Funfschilling, H.Z. Li. Effects of the injection period on the rise velocity and shape of a bubble in a non-Newtonian fluid, Chemical Engineering Research and Design 84(10) (2006) 875–883. doi: 10.1205/cherd.01229.
[70] X. Frank, H.Z. Li, Negative wake behind a sphere rising in viscoelastic fluids: A lattice Boltzmann investigation, Phys. Rev. E 74 (5) (2006) 1–9, https://doi.org/10.1103/PhysRevE.74.056307.
[71] M.K. Hausmann, P.A. Rühs, G. Siqueira, J. Läuger, R. Libanori, T. Zimmermann, A.R. Studart, Dynamics of Cellulose Nanocrystal Alignment during 3D Printing, ACS Nano 12 (7) (2018) 6926–6937, https://doi.org/10.1021/acsnano.8b02366.
[72] R. Kádár, M. Fazilati, T. Nypelö, Unexpected microphase transitions in flow towards nematic order of cellulose nanocrystals, Cellulose 27 (4) (2020) 2003–2014, https://doi.org/10.1007/s10570-019-02888-x.
[73] R. Kádár, S. Spirk, T. Nypelö, Cellulose nanocrystal liquid crystal phases: Progress and challenges in characterization using rheology coupled to optics, scattering, and spectroscopy, ACS Nano 2021 15 (5), 7931-7945.
[74] T. Rosén, N. Mittal, S.V. Roth, P. Zhang, F. Lundell, L.D. Söderberg, Flow fields control nanostructural organization in semiflexible networks, Soft Matter 16 (23) (2020) 5439–5449, https://doi.org/10.1039/C9SM01975H.
[75] C. Brouzet, N. Mittal, F. Lundell, L.D. Söderberg, Characterizing the orientational and network dynamics of polydisperse nanofibers on the nanoscale, Macromolecules 52 (6) (2019) 2286–2295, https://doi.org/10.1021/acs.macromol.8b02714.
[76] K.M.O. Håkansson, A.B. Fall, F. Lundell, S. Yu, C. Krywka, S.V. Roth, G. Santoro, M. Kvick, L. Prahl Wittberg, L. Wågberg, L.D. Söderberg, Hydrodynamic alignment and assembly of nanofibrils resulting in strong cellulose filaments, Nat. Commun. 5 (1) (2014) 4018, https://doi.org/10.1038/ncomms5018.